Inside the electrode: Looking at cycling products in Li/O₂ batteries

Matthias Augustin*[1], Per Erik Vullum[2], Fride Vullum-Bruer[1], Ann Mari Svensson[1]

[1] Department of Material Science and Engineering, Norwegian University of Science and

Technology (NTNU), Høgskoleringen 1, NO-7491 Trondheim, Norway

[2] SINTEF Industry, NO-7491 Trondheim, Norway

* Corresponding author

email: matthias.augustin@ntnu.no

Abstract

This work investigates the impact of electrochemical reactions and products on discharge capacity and cycling stability with electrolytes based on two common solvents – tetraethylene glycol dimethyl ether (TEGDME) and dimethyl sulfoxide (DMSO).

Although the DMSO-based electrolyte exhibits better initial electrochemical properties compared to that based on TEGDME, e.g., higher discharge capacity and potential, the use of TEGDME results in a significantly better cycling stability.

Scanning electron microscopy (SEM) and X-ray diffraction (XRD) investigations of the gas diffusion electrodes (GDE) after first discharge reveal a considerable difference in discharge product morphology. With DMSO as solvent one high-potential reduction process leads to the formation of crystalline lithium peroxide (Li_2O_2) particles on the cathode surface area. SEM imaging of GDE cross-sections depicts that the (non-crystalline) product film formation at lower potentials during discharge with the TEGDME-based electrolyte results in a GDE pore clogging close to the O_2 inlet, so that gas transport is hindered and the discharge ends at an earlier point. The higher cycling stability with LiTFSI/TEGDME, however, is attributed to (i) the apparently complete recovery of the GDE active surface by recharge and (ii) different parasitic reactions resulting in the formation of side product particles rather than films.

1. Introduction

The interest in secondary Li/O$_2$ batteries has grown rapidly over the past two decades, as they exhibit a practically achievable specific energy of about 1,700 Wh/kg, which equals that of gasoline and is well beyond those of conventional battery systems [1,2].

The oxygen reduction reaction (ORR) is the discharge reaction taking place at the cathode side of the Li/air cell, for which the following general sequence of reactions have been proposed by Laoire *et al.* to take place in non-aqueous electrolytes [3,4]:

$$O_2 + Li^+ + e^- \rightarrow LiO_2 \tag{1}$$

$$LiO_2 + Li^+ + e^- \rightarrow Li_2O_2 \tag{2}$$

$$2\,LiO_2 \rightarrow Li_2O_2 + O_2 \tag{3}$$

$$Li_2O_2 + 2\,Li^+ + 2\,e^- \rightarrow 2\,Li_2O \tag{4}$$

During discharge a one-electron reduction of oxygen to superoxide LiO$_2$ (eq. 1) is followed by a further one-electron reduction and/or a chemical disproportionation of LiO$_2$ to lithium peroxide Li$_2$O$_2$ (eqs. 2 and 3) [5–7]. This mechanism was confirmed by *in situ*-spectroscopic studies revealing LiO$_2$ as ORR intermediate as well as its subsequent chemical disproportionation Li$_2$O$_2$ (eq. 3) [8]. A further two-electron reduction of Li$_2$O$_2$ takes place at lower potentials and results in the formation of lithium oxide Li$_2$O (eq. 4) [9]. Discharge to Li$_2$O would increase the theoretical specific energy of the aprotic Li/air system by about 800 Wh/kg [10]. However, Li$_2$O is electrochemically irreversible and hence can only be oxidized at large overpotentials, so that Li$_2$O$_2$ (with a reversible redox potential of $E^0 = 2.96$ V [11,12]) is the desired discharge product [4,13].

The major drawback of this seemingly simple system, however, is the reactivity of the organic electrolytes with almost all battery components (including cycling intermediates and products) and hence several decomposition reactions. The resulting side products are deposited in the GDE pores together with the reaction products, leading to a minimized active electrode surface and ultimately cell failure upon continued cycling [14].

A stable electrolyte has not been found yet, although some solvents are proposed to exhibit sufficient stability under laboratory conditions. The search for a suitable electrolyte for applications of the Li/air system is complicated by the very different properties the electrolyte solvent has to exhibit. The most important of these are (i) stability against Li metal, (ii) stability against the O_2^- radicals produced during the ORR and (iii) low volatility for long-term applications. Further properties of a suitable solvent include high O_2 solubility and a stabilizing effect of the intermediate product LiO_2 to prevent a direct formation of Li_2O_2 or even Li_2O. In a previous study Laoire *et al.* investigated possible electrolyte solvents with respect to their capability of LiO_2 formation by considering Pearson's HSAB (hard soft acids bases) concept [4], which describes chemical species as Lewis acids or bases by their strengths for electron acceptance. The Li^+ ions taking part in the formation of the ORR products are strong acids and will preferably react with the strong bases O_2^{2-} and O^{2-} to form Li_2O_2 and Li_2O. The desired LiO_2 species, however, is formed with the weak base O_2^-. This reaction can be achieved by weakening the acidity of Li^+ ions by formation of $[Li(sovent)_n]^+$ compounds. Therefore, it is important to use solvents with a high Lewis basicity indicated by a high Gutmann donor number (DN).

Two of the currently most applied organic solvents are dimethyl sulfoxide (DMSO) and tetraethylene glycol dimethyl ether (TEGDME) due to their stability with respect to the components in the system and the necessary potential window [15–18]. DMSO and TEGDME are typical examples for high and low Lewis basicity solvents with DNs of 29.8 and 16.6,

respectively. In accordance to the HSAB theory Laoire *et al.* reported a better stabilization of LiO_2 by DMSO [4]. Supporting these findings, several groups observed toroidally shaped Li_2O_2 particles on the surface of discharged electrodes with different microscopy methods [15,19]. Li_2O_2 toroids are a common discharge product of the so-called solution growth pathway proceeding *via* an EC mechanism [20]: O_2 is reduced to O_2^-, which is dissolved and forms LiO_2. The solvated LiO_2 intermediates subsequently disproportionate to solid Li_2O_2 particles with different morphologies (which depend on the nature of the electrolyte) [21–23]. The ORR proceeds majorly *via* this mechanism when high DN electrolyte solvents are used and/or discharge parameters, such as low discharge current densities and low overpotentials, are applied [24–27]. With low DN solvents and/or high current densities and overpotentials, the discharge reaction proceeds *via* the surface growth pathway. As less of the above-mentioned $[Li(solvent)_n]^+$ complexes are formed in weakly basic solvents, this pathway results in a Li_2O_2 film by electrochemical formation of adsorbed LiO_2 and its subsequent reduction (EE mechanism) or disproportionation (EC mechanism) to Li_2O_2 on the cathode surface (see also eqs. 1 and 2) [25,28–30]. However, these mechanisms represent extreme cases. Previous electrochemical studies showed that in reality the ORR in high DN electrolytes will always proceed to a certain degree *via* the surface growth pathway, as not all O_2^- intermediates are dissolved before they are further reduced [20,31].

Whereas the discharge mechanisms are relatively well understood, the detailed processes of the oxygen evolution reaction (OER) occurring during recharge are still subject of debate. Amorphous Li_2O_2 has been shown to be oxidized at lower potentials than crystalline Li_2O_2, which is formed as Li_2O_2 toroids and particles *via* the solution growth pathway [32,33]. In general Li_2O_2 is oxidized to O_2 either by initial delithiation *via* $Li_{2-x}O_2$ or LiO_2 at low potentials (i.e., the reverse eq. 2) [34,35] and/or a direct two-electron step without the formation of LiO_2 as an intermediate species [8]. Recent reports investigating the recharge processes have shown

that singlet oxygen evolving during complete Li_2O_2 oxidation at potentials ≥ 3.55 V are at least one of the reasons for carbon cathode and probably also electrolyte decomposition [36,37].

A majority of the works conducted in order to understand the detailed reaction mechanisms in the Li/O_2 system has been performed in model (i.e., half-cell) systems, where lithium metal is not present on the anode side and/or model cathodes like gold or glassy carbon are used. Additionally, reports investigating reactions and reaction products of the two discharge pathways in suitable electrolytes while using the same cycling parameters are rare. In order to obtain such insight, this work investigates the influence of solution growth- and surface growth-mediating electrolytes based on DMSO and TEGDME, respectively, on the formation of cycling products in a porous carbon cathode. A combination of electrochemical characterization and *post mortem* (cross-sectional) SEM and XRD analysis of the cathodes at different states of discharge and charge provides information about the observed detected products and their effect on the electrochemical performance in a full cell system.

2. Experimental

2.a) <u>Materials</u>

TGP-H-60 Toray carbon paper (PTFE treated) was purchased from Alfa Aesar and Vulcan® XC72 carbon black from Cabot Corp. Polyvinylidene difluoride (PVDF, $\geq 99\%$) and tetraethylene glycol dimethyl ether (TEGDME, 99%) were obtained from AME Energy Co., Ltd. and Acros Organics, respectively. N-methyl-2-pyrrolidone (NMP, anhydrous, 99.5%), 1,2-dimethoxyethane (DME, anhydrous, 99.5%, inhibitor-free), lithium

bis(trifluoromethanesulfonyl)imide (LiTFSI, 99.95% trace metals basis), lithium nitrate (LiNO$_3$, 99.99% trace metals basis), lithium perchlorate (LiClO$_4$, battery grade, dry, 99.99% trace metals basis) and dimethyl sulfoxide (DMSO, anhydrous, $\geq$ 99.9%) were purchased from Sigma Aldrich. All chemicals were used as purchased without further purification.

2.b) Electrolyte & electrode preparation

1 M Li$^+$ ion-containing mixtures of LiTFSI/DMSO, LiTFSI/TEGDME, (1 LiNO$_3$: 1 LiTFSI)/ TEGDME and LiClO$_4$/TEGDME were prepared in a glove box (Mbraun) in an Ar atmosphere with < 0.1 ppm H$_2$O and < 0.1 ppm O$_2$ content. The electrodes were fabricated by casting a paste containing Vulcan® XC72 carbon black and a PVDF/NMP solution onto the TGP-H-60 Toray carbon paper. The C/PVDF ratio in the paste was 9:1, the wet-casting thickness 120 µm. The wet electrode cast was pre-dried at 60°C for 45 min to remove residual NMP. Subsequently the cast was heated overnight to 85°C under vacuum and transferred to a glove box with argon atmosphere, where the gas diffusion electrodes (GDEs) with $d = 16$ mm were cut from the cast. The carbon black loading of the electrodes was 2.03 mg ± 0.10 mg.

2.c) Cell assembly & electrochemical measurements

The test cells were assembled in Ar atmosphere using ECC-Air setups (EL-CELL® GmbH) with Li metal discs as anodes/counter electrodes, Li metal as reference electrodes and GDEs as cathodes/working electrodes. In the setup glass fiber separators soaked with 325 µL of electrolyte were placed between the Li and GDE discs.

All electrochemical measurements were carried out at ambient temperature with a Reference 600 potentiostat (Gamry Instruments) and a VMP-300 multipotentiostat (Bio-Logic Science Instruments). Linear sweep voltammetry (LSV) was carried out in Ar atmosphere with a scan rate of in a potential range of $\Delta E = 2.0$ V – 4.5 V vs. Li/Li$^+$. For all other electrochemical measurements the test cells were purged with a constant O_2 gas flow of 4 mL/min at a pressure of 3 bar (gas purity: 5.0, AGA AS). Galvanostatic cycling and cyclic voltammetry (CV) experiments were performed with a discharge/charge current density of $i = 75$ mA g_C^{-1} and a potential scan rate of $v = 0.1$ mV s^{-1}, respectively, in a potential window of $\Delta E = 2.0$ V – 4.5 V vs. Li/Li$^+$. Differential capacity plots were obtained from galvanostatic cycling experiments with a resolution of $\Delta E = 0.1$ mV.

All electrochemical measurements were carried out at least three times to check for reproducibility. Average values and standard deviations are displayed in the respective figures unless otherwise noted.

2.d) <u>Characterization methods</u>

Scanning electron microscopy (SEM) was carried out using a FEI Helios G4 UX dual-beam focused ion beam – scanning electron microscope (FIB-SEM) with an acceleration voltage of 15 kV. GDE cross-sections were made *in situ* inside the FIB with the Ga$^+$ ion beam. Prior to making a cross-section, carbon protection layers (first, a thin layer deposited with electron beam-assisted deposition and, second, a thicker layer deposited by ion beam-assisted deposition) were deposited on the surface of the region of interest.

X-ray diffraction (XRD) measurements were performed with a Bruker D8 Focus diffractometer operating with Cu K$_\alpha$ radiation (wavelength λ_{Cu} = 0.15418 nm), a Bragg-Brentano (θ-2θ) geometry and a LynxEye™ SuperSpeed Detector using an inert atmosphere sample holder.

Transmission electron microscopy (TEM) was carried out using a XXX with an acceleration voltage of 80 kV.

For sample preparation the battery test cell was disassembled in a glove box, the GDE was removed and rinsed three times with DME in order to remove residues of LiTFSI and the respective solvent. The GDE was then left in vacuum for 5 min for a removal of the DME by evaporation. For SEM measurements the sample GDE was placed on a sample holder and transferred into the FIB-SEM vacuum chamber with a maximum air exposure time of ca. 2 min. For XRD measurements the GDE was placed on a Si wafer in the inert atmosphere sample holder and transferred to the diffractometer chamber thus excluding any exposure to air. For TEM measurements the GDE was put in DME and ultrasonificated for 10 s. A drop of the GDE/DME dispersion was applied onto a carbon-coated copper TEM grid, which was placed in an inert atmosphere TEM sample holder in the glovebox. Subsequently, the sample holder was transferred into the TEM vacuum chamber without any exposure to air.

3. Results & Discussion

The electrochemical properties of the two electrolytes LiTFSI/TEGDME and LiTFSI/DMSO were investigated by galvanostatic cycling. Subsequently, the products obtained during discharge and charge were analyzed by *ex situ* characterization at different states of (dis)charge.
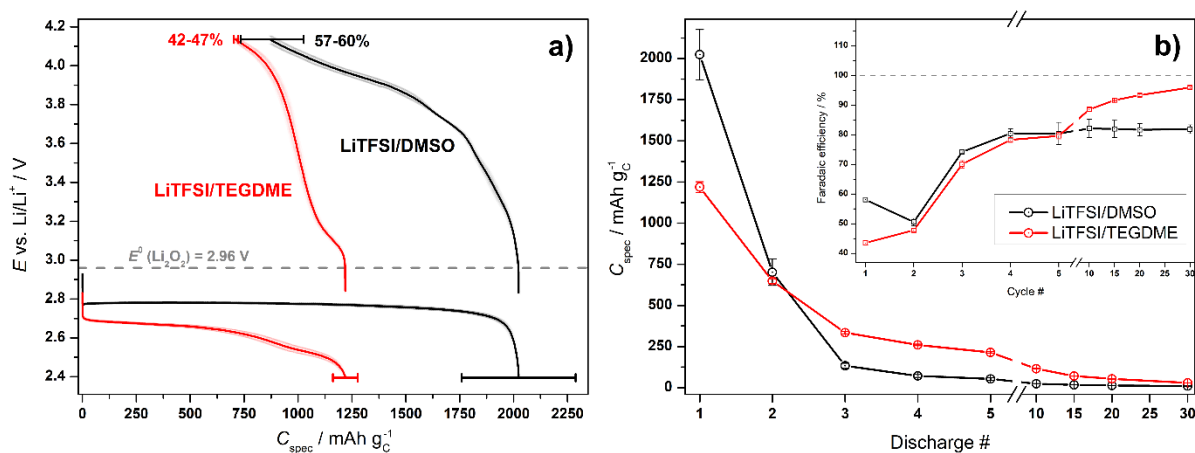
Figure 1: (a) Averaged first galvanostatic discharge/charge cycles with LiTFSI/DMSO (black) and LiTFSI/TEGDME (red); $i = 75$ mA g_C^{-1}; the error bars denote standard deviations; (b) discharge capacities and Faradaic efficiencies (inset) obtained from galvanostatic cycling with LiTFSI/DMSO (black) and LiTFSI/TEGDME (red).

The galvanostatic cycling data presented in Fig. 1 are in line with results obtained with CV measurements, which are presented in the Supporting Information, Fig. S1. In the first cycle LiTFSI/DMSO exhibits a lower discharge overpotential, whereas an initially lower recharge overpotential is observed with LiTFSI/TEGDME (see Fig. 1.a). The DMSO-based electrolyte also exhibits a larger initial discharge capacity of 2024 ± 152 mAh g_C^{-1}, which is very close to that of ca. 2200 mAh g_C^{-1} reported for a discharge with LiTFSI/DMSO using CNT cathodes and comparable current densities [38]. The lower discharge capacities obtained with LiTFSI/TEGDME are in good agreement to the lower cathodic current densities in the CV (see Fig. S1). The subsequent discharge capacities decrease exponentially (see Fig. 1.b), which is most probably also – but not solely – connected to the incomplete recharges with both electrolytes visible from the Faradaic efficiencies (see inset in Fig. 1.b).

However, this cannot be the only reason, as – regarding the cycling stability – LiTFSI/TEGDME performs better than LiTFSI/DMSO, despite a lower average initial recharge of ca. 45% compared to 57-60% with DMSO as solvent. This is also observed in the CV measurements, which show that the cycle stability with the TEGDME-based electrolyte is – if also not sufficiently high – at least higher than that with LiTFSI/DMSO (see Fig. S1). Hence, the cause for the difference regarding the cyclability with both electrolytes is already evident in the first cycle, which is confirmed by XRD measurements (see Fig. 2).
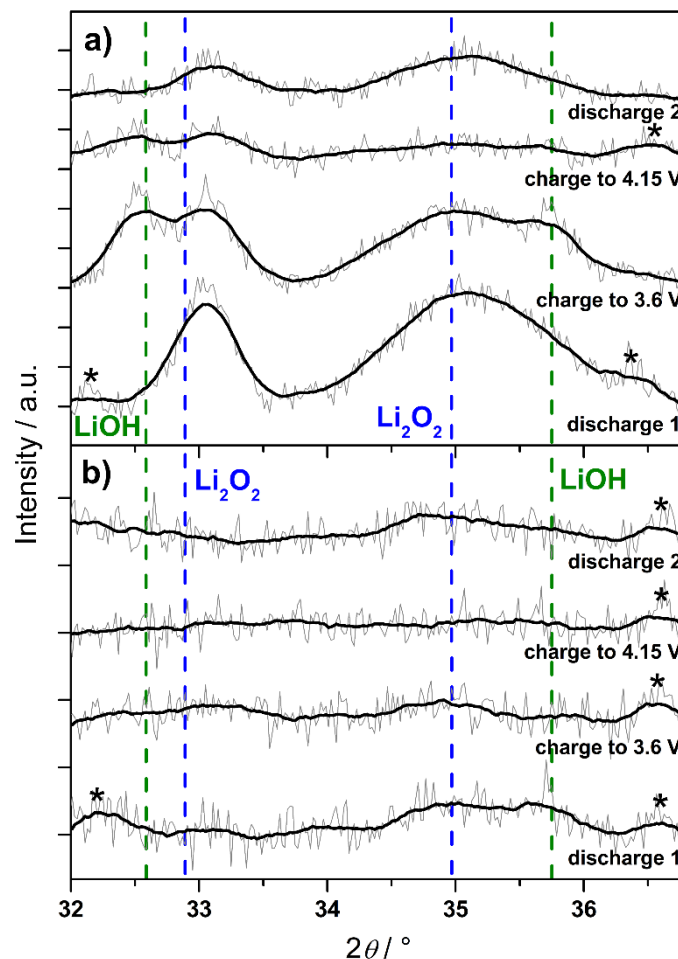
Figure 2: X-ray diffractograms of GDEs at different states of charge with (a) LiTFSI/DMSO and (b) LiTFSI/TEGDME; dashed blue and green lines denote literature reflections of Li_2O_2

[39] and LiOH [40], respectively, black stars denote literature reflections of LiTFSI [41]; grey lines are diffractograms as measured, black lines are moving average to guide the eye.


The presence of crystalline Li_2O_2 is clearly visible in the XRD of the GDE after full discharge with LiTFSI/DMSO but only indicated by a weak reflection when using the TEGDME-based electrolyte. Further reflections show the presence of LiOH in the GDE after discharge with LiTFSI/TEGDME (weak) as well as after discharge and initial recharge to 3.6 V with DMSO as solvent (strong). This compound is commonly associated with the decomposition of electrolyte solvents [42–44], which has already been suggested in the previous discussion of the electrochemical measurements. The presence of LiOH is likely to influence the electrochemical performance in two different ways: First, indirectly, as LiOH is most probably the product of electrolyte decomposition, the electrolyte will react completely with progressing time and the battery cell dries out. Second, the presence of crystalline LiOH as side product leads to electrode surface blockage and hence less electrode area, which is active for electrochemical reactions. The XRD measurement after charge to 4.15 V (see Fig. 2) shows that crystalline LiOH was not oxidized completely, so that a repeated formation and incomplete oxidation of crystalline LiOH might be one of the reasons for the low cycling stability with both electrolytes. In order to distinguish between electrochemical and chemical products identified in Fig. 2 XRD measurements of GDEs were performed after 13 h and 20 h of discharge with TEGDME- and DMSO-based electrolytes, respectively (see Fig. 3).
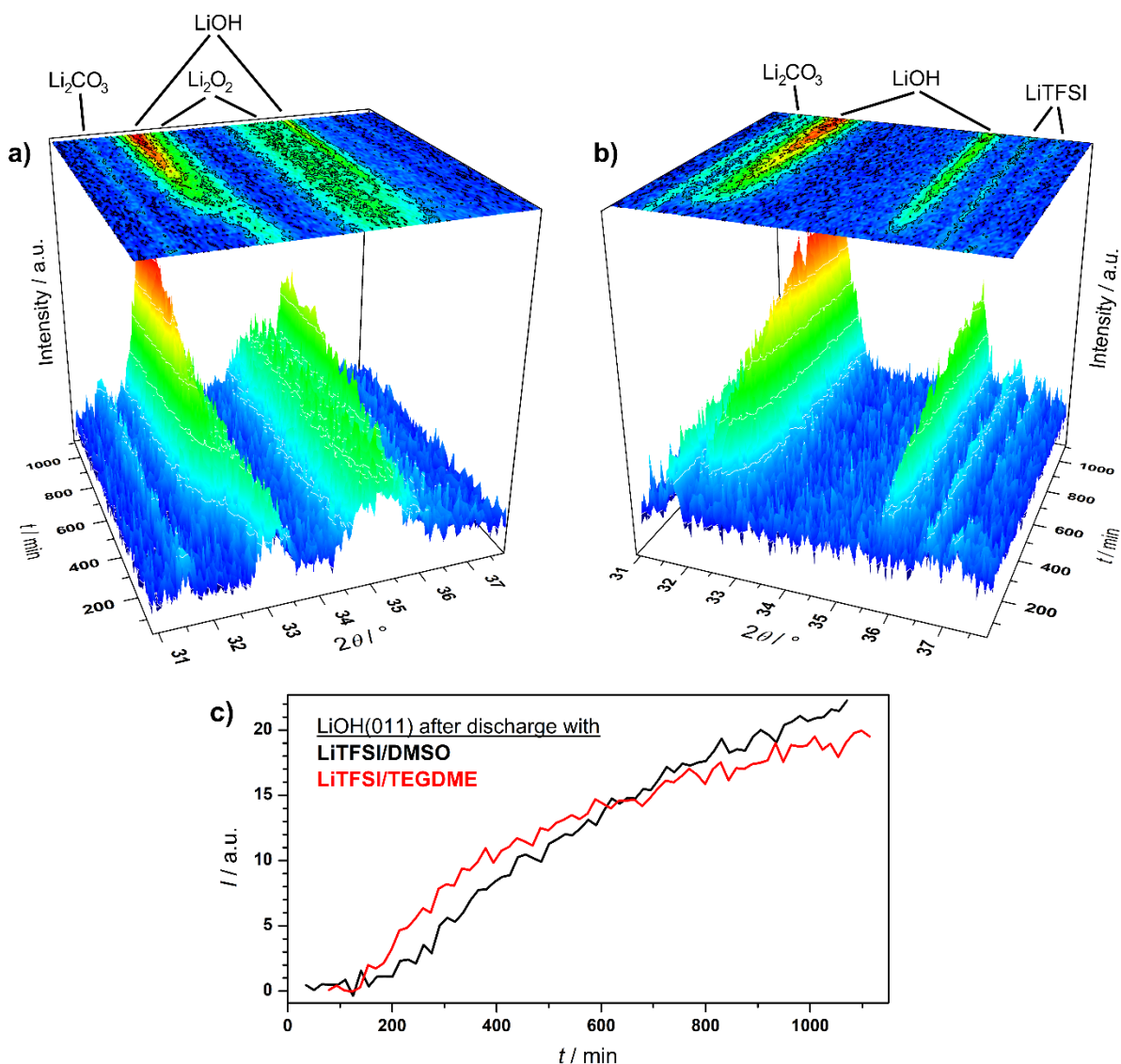
Figure 3: X-ray diffractograms of GDEs after battery disassembly showing the time-dependent formation of LiOH in GDEs discharged with (a) LiTFSI/DMSO and (b) LiTFSI/TEGDME; (c) intensity of the LiOH(011) reflection detected at ca. 32.6° after discharge with LiTFSI/DMSO (black) and LiTFSI/TEGDME (red).

The XRD results depicted in Fig. 3 show the additional presence of Li_2CO_3 in the GDE after discharge with both electrolytes, which has also been reported to be a product of parasitic reactions during cycling[44–46]. As its presence is observed in both, LiTFSI/DMSO and

13

LiTFSI/TEGDME, it is likely that Li_2CO_3 is the product of a side reaction between LiO_2 and/or Li_2O_2 with the carbon particles of the GDE, which was recently shown in a study by Belova *et al.* for non-porous carbons of different crystallinities[47]. However, LiOH is not present in the GDE 30 min after discharge cut-off with both electrolytes but is instead the product of a time-dependent chemical reaction after battery disassembly. The intensity of the LiOH(011) reflection detected at ca. 32.6° shows sharp increases ca. 200 min and ca. 140 min after end of discharge with LiTFSI/DMSO and LiTFSI/TEGDME, respectively (see Fig. 3.c). LiOH is proposed here to be formed from chemical reactions between Li_2O_2 and the respective solvent by deprotonation (DMSO) and proton-mediated degradation (TEGDME)[2,48–50], which – based on the timeline of Fig. 3.c) – is very likely to happen during uninterrupted discharge, i.e., without discharge time limitation. As the formation of LiOH proceeds faster after discharge with LiTFSI/TEGDME, and amorphous Li_2O_2 was found to be more reactive than crystalline Li_2O_2 [26], amorphous Li_2O_2 is most likely the main product after discharge with the TEGDME-based electrolyte. This assumption is further supported by the SEM images shown in Figs. 4.a) and 5.a), which depict the presence of product particles on the GDE surface after discharge with LiTFSI/DMSO and that of layered products after discharge with LiTFSI/TEGDME, respectively.

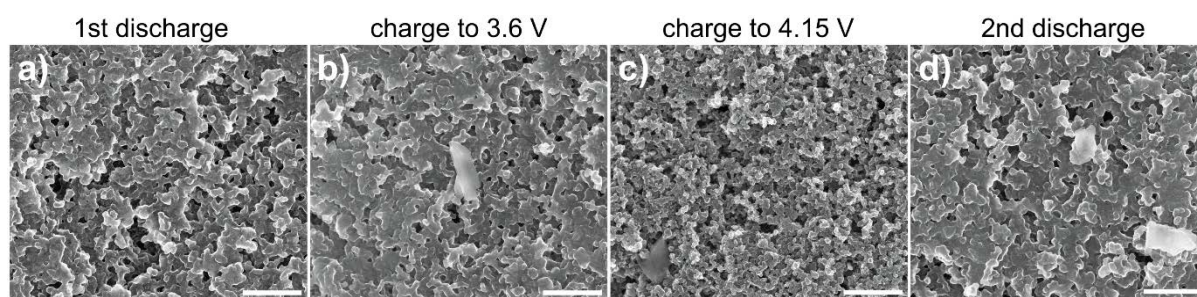| 1st discharge | charge to 3.6 V | charge to 4.15 V | 2nd discharge |
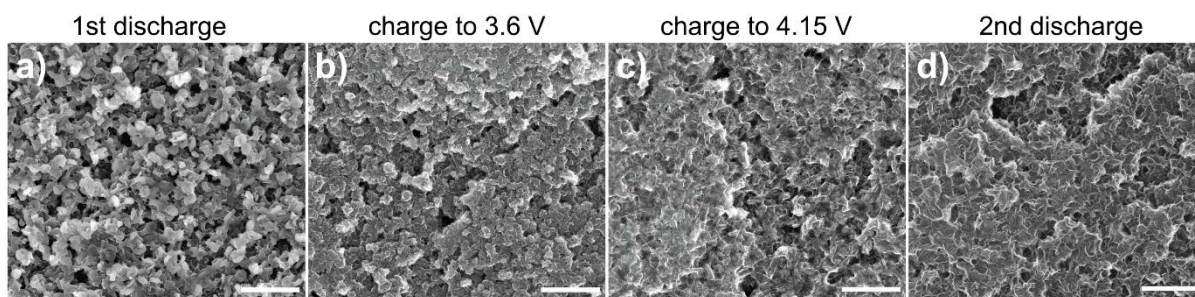
Figure 4: SEM images of GDE surfaces after (a) initial discharge, (b) first charge to ca. 3.6 V, (c) first complete recharge to 4.15 V and (d) second discharge with LiTFSI/DMSO; scale bars: 1 µm.

After complete discharge with LiTFSI/DMSO the GDE surface, i.e., the solid/electrolyte reaction interface, is covered with toroidal particles with diameters between 180 nm – 200 nm and several "donut"-shaped particles with diameters of up to 350 nm (see Fig. 4.a) and compare to the SEM images of a pristine GDE in Fig. S2). These particles were reported by several groups to show the solution growth pathway product Li_2O_2 in different states of growth [22,23,51], and are most likely related to the crystalline signals observed in the XRD measurements depicted in Figs. 2.a) and 3.a). The porous GDE structure is almost completely clogged by product deposits, which is also the case after discharge with LiTFSI/TEGDME (see the contrast between the dark carbon network and the brighter discharge product in the cross-section SEM images depicted in Figs. 6.a) and 7.a). The remaining open pores reveal a view into the inside of the otherwise blocked carbon electrodes where "donut"-shaped particles show the presence of the crystalline Li_2O_2 product also inside the GDE.

The electrochemical processes underlying the formation of these discharge products are shown in the differential capacity plots in Fig. 8. The first discharge with LiTFSI/DMSO consists of one reduction process at 2.77 V (see Fig. 8.a) assigned to the initial step of the solution growth pathway – the reduction of O_2 to O_2^- [20,27]. As the subsequent formation of solvated LiO_2

and Li_2O_2 particles by LiO_2 disproportionation are chemical reactions, they are not detectable by electrochemical methods. The resulting products – toroidal and "donut"-shaped particles –, however, are visible in the SEM images depicted in Fig. 4.a). Previous studies pointing out simultaneous product formation *via* solution growth and surface growth pathways[20,31] are supported by the observation of the pore-clogging "bulk" product in the GDE cross-sections aside from the already discussed particles after discharge with both electrolytes (see Figs. 6.a) and 7.a).

Figure 5: SEM images of GDE surfaces after (a) initial discharge, (b) first charge to ca. 3.6 V, (c) first complete recharge to 4.15 V and (d) second discharge with LiTFSI/TEGDME; scale bars: 1 μm.

The GDE surface after discharge with LiTFSI/TEGDME (see Fig. 5.a) is completely covered by a product layer comparable to that found by Wong *et al.* on graphitized multi-walled carbon nanotubes after discharge in $LiClO_4$/TEGDME [52]. Furthermore, this observation is in good agreement with reports proposing that low DN electrolyte solvents enhance the Li_2O_2 surface growth pathway resulting in film rather than particle formation [30,53,54]. As previously mentioned, however, the ORR takes place most likely *via* both surface growth and solution growth pathways also with TEGDME-based electrolyte, which was reported by Ryu *et al.* [55]

and is directly visible in Fig. 7.a). The porous GDE structure is almost completely clogged by apparently amorphous "bulk" product but also "donut"-shaped particles, which are similar in number and morphology to those observed after discharge with LiTFSI/DMSO (see Fig. 6.a). Another reason which might contribute to the presence of this product mixture in the pores might be the influence on the processes by GDE properties, such as carbon particle as well as pore diameters and pore volume as proposed by Xue *et al.* [56,57].

Next to the presence of a Li_2O_2 film as the major discharge product on the GDE surface another difference is the extreme electron beam-sensitivity of the products present after discharge with LiTFSI/DMSO compared to those present after discharge with the TEGDME-based electrolyte (see the SEM images in Figs. S3 and S4 as well as the TEM image in Fig. S5). This points to the formation of more stable products during discharge with the latter electrolyte and hence *via* a predominant surface growth ORR pathway.

The differential capacity plot depicted in Fig. 8.b) shows that the discharge with LiTFSI/TEGDME contains two reduction processes at 2.67 V and 2.54 V, which are attributed to the Li_2O_2 formation *via* solution growth and surface growth pathways, respectively. As TEGDME is a low DN solvent, the latter pathway has a larger contribution compared to LiTFSI/DMSO, which is also visible in the initial discharge curves depicted in Fig. 1.a). That the high-potential process (solution growth pathway) with LiTFSI/TEGDME is detected at lower potentials than in LiTFSI/DMSO (see also CV measurements in Fig. S1) is probably the result of the significantly lower O_2/O_2^- standard redox potential in ethers compared to DMSO [58]. Further support for this assumption is obtained when the Li^+ ion conducting salt in the TEGDME-based electrolyte is changed either by replacement of LiTFSI by $LiClO_4$ or by addition of $LiNO_3$ to LiTFSI. Both ways should lead to a change of the discharge reaction pathway toward predominant Li_2O_2 particle formation: For $LiNO_3$ recent reports have already shown an at least partial change of discharge mechanism from film to particle formation *via*

solvated LiO_2 in ether-based electrolytes [24,59–61]. In case of $LiClO_4$ this effect might be caused by the slightly higher DN compared to LiTFSI [62]. From the cycling experiments depicted in Fig. S6 several observations attributed to solution growth pathways during discharge support the assumptions made above. A (partial) replacement of LiTFSI either of the salts results in (i) significantly increased initial discharge potentials and capacities (see Fig. S6.a), (ii) decreased cycling stabilities (see Fig. S6.b) as well as (iii) the decrease/disappearance of the low-potential (surface-growth) during initial discharge (see Figs. S6.c) and S6.d). All these electrochemical characteristics are in agreement with those observed with LiTFSI/DMSO and thus can be attributed to a predominance of the solution growth pathway resulting mainly in Li_2O_2 particle formation. Hence, this process is detected at lower potentials in TEGDME-based electrolytes compared to DMSO-based electrolytes.
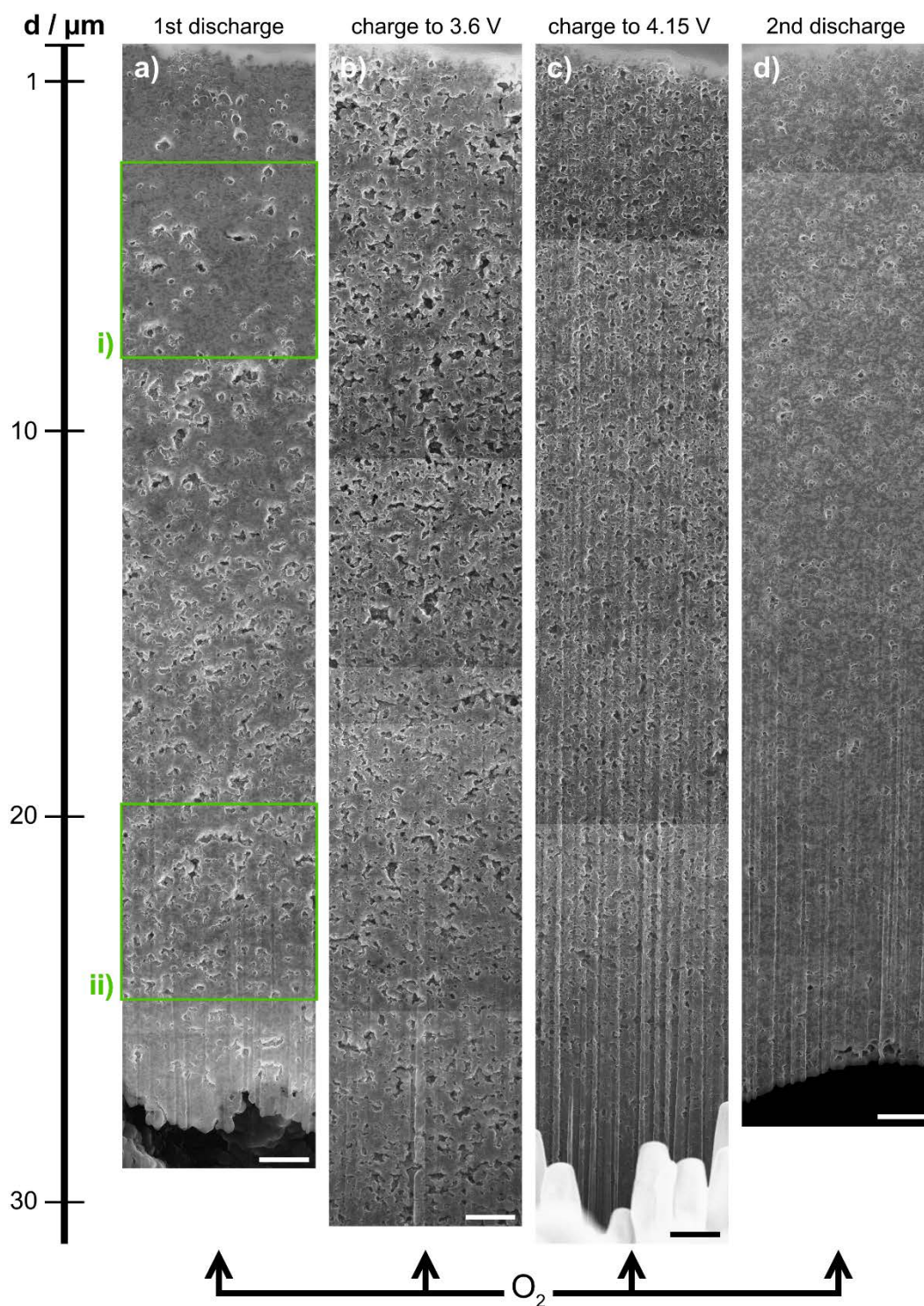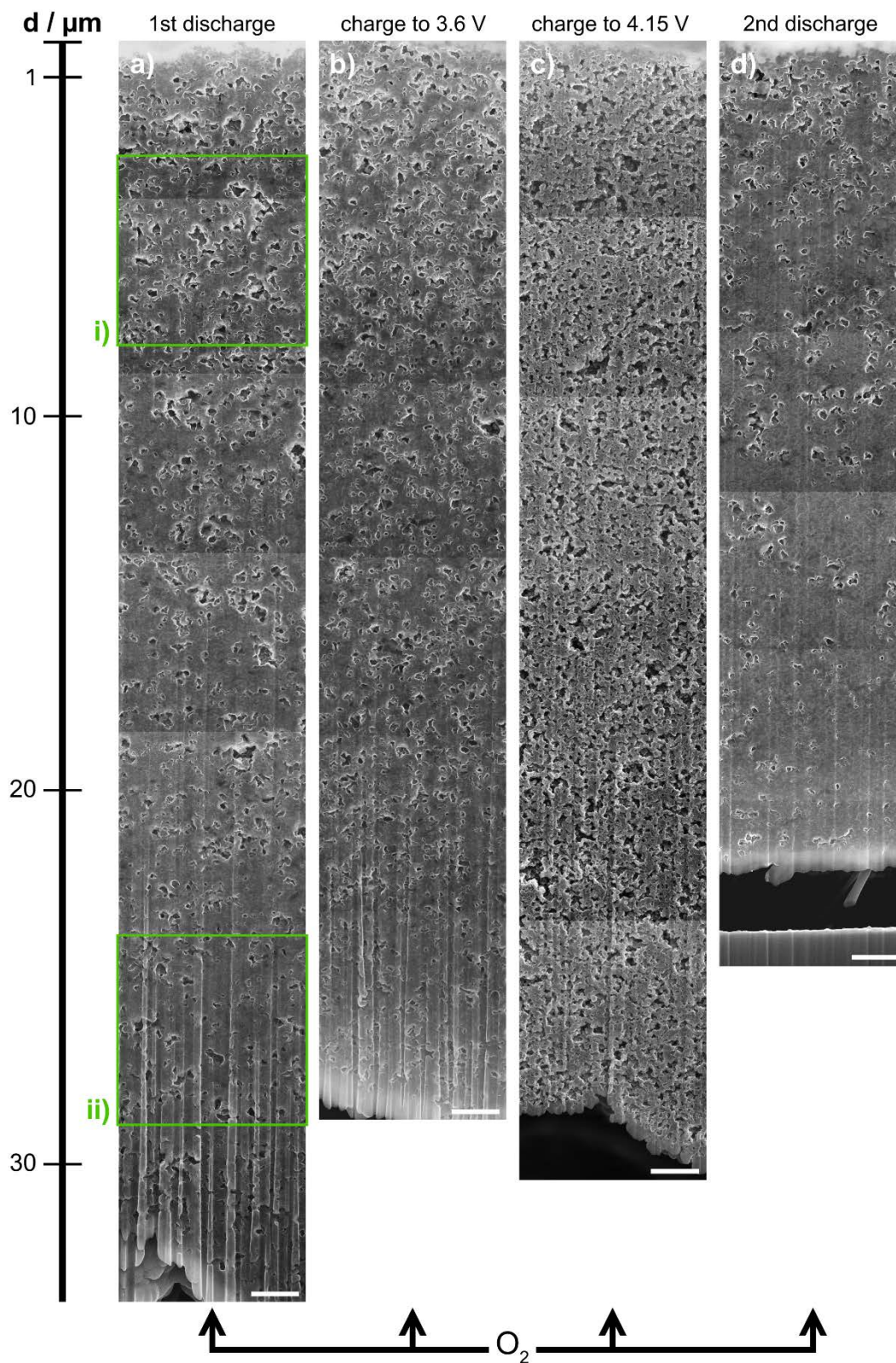
Figure 6: Cross-section SEM images showing GDE depth profiles after (a) initial discharge, (b) first charge to ca. 3.6 V, (c) first complete recharge to 4.15 V and (d) second discharge with LiTFSI/DMSO; scale bars: 1 µm; the homogeneous contrast at the top of each image is the C protection layer deposited on the surface of the GDE to avoid ion-beam damage in the region

of interest; the abrupt, horizontal changes in contrast and brightness are artefacts from stitching several SEM images together.

SEM images depicting cross-sectional depth profiles of GDEs discharged with both electrolytes are shown in Figs. 6.a) and 7.a). Compared to the cross-section of a pristine electrode (see Fig. S2.b) the pore clogging by discharge products is obvious (see also the "donut"-shaped particles in the open pores). However, there is one significant difference: discharge with LiTFSI/DMSO resulted in a product gradient decreasing from the separator side of the GDE to the O_2 inlet side (compare green squares (i) and (ii) in Fig. 6.a). The direct opposite is observed after discharge with LiTFSI/TEGDME, i.e., less product deposits are found on the separator side (compare green squares (i) and (ii) in Fig. 7.a). This is most likely directly related to the different discharge pathways. A saturation of the electrolytes with incoming O_2 provides enough educt concentration for both reduction mechanisms. Subsequent to the formation of the O_2^- intermediates by the initial reduction step adsorbed LiO_2 is produced in LiTFSI/TEGDME, whereas solvated LiO_2 is the predominant intermediate in LiTFSI/DMSO. The adsorbed LiO_2 is further reduced at the site of initial reduction, whereas the solvated compound has a higher probability to be transported through the electrode pores to the separator side with the LiO_2 concentration gradient as driving force. Hence, the pores on the separator side of the GDE are the primary deposition sites during discharge with LiTFSI/DMSO, the GDE pores close to the O_2 inlet the favored sites for Li_2O_2 film formation during discharge with a TEGDME-based electrolyte.

Figure 7: Cross-section SEM images showing GDE depth profiles after (a) initial discharge, (b) first charge to ca. 3.6 V, (c) first complete recharge to 4.15 V and (d) second discharge with LiTFSI/TEGDME; scale bars: 1 µm; the homogeneous contrast at the top of each image is the

C protection layer deposited on the surface of the GDE to avoid ion-beam damage in the region of interest; the abrupt, horizontal changes in contrast and brightness are artefacts from stitching several SEM images together.
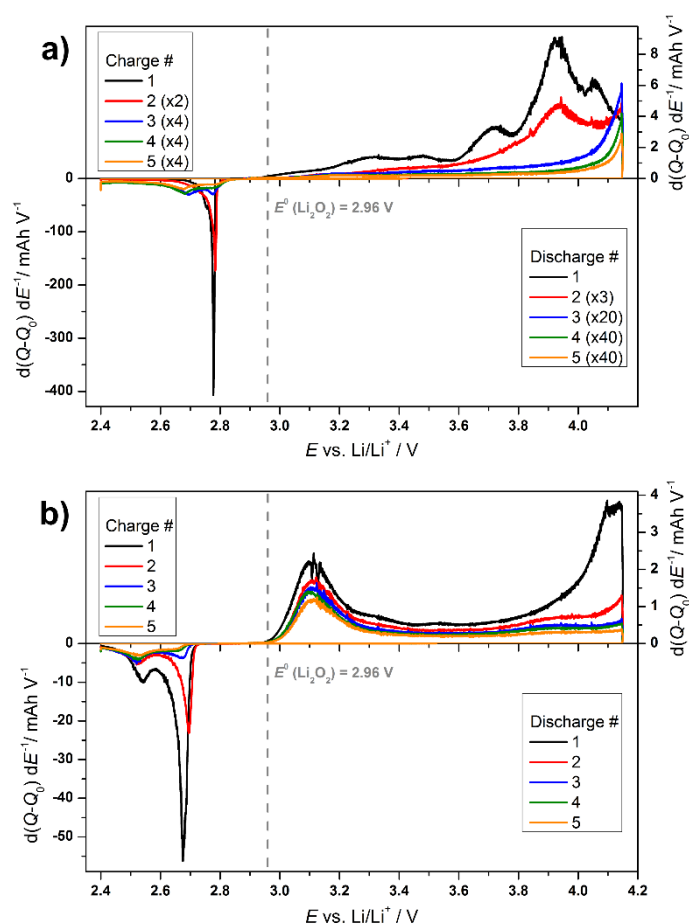
Figure 8: Representative differential capacity plots obtained from the five initial galvanostatic cycles with (a) LiTFSI/DMSO and (b) LiTFSI/TEGDME.

Hence, the larger initial discharge capacity and higher ORR potentials when using LiTFSI/DMSO as electrolyte are attributed to the difference in Li_2O_2 formation pathways during discharge. Whereas the presence of crystalline Li_2O_2 and toroidal/"donut"-shaped particles dominates the GDE surface after discharge with LiTFSI/DMSO, the use of TEGDME

as solvent results in the formation of an apparently amorphous layer as major discharge product. The GDE pores were almost completely clogged with discharge product with both electrolytes. Li_2O_2 predominantly forms close to the O_2 inlet with LiTFSI/TEGDME, which might well be another reason for the lower discharge capacity obtained with low DN electrolytes. Li_2CO_3 was identified as side product after discharge, and LiOH was shown to form chemically during discharge with both electrolytes.

During first recharge with LiTFSI/DMSO three minor oxidation processes are observed at low potentials of 3.1 V (very small), 3.3 V and 3.5 V as well as three major ones at higher potentials of 3.7 V, ca. 3.95 V and 4.05 V (see Fig. 8.a).

The according SEM images after recharge to ca. 3.6 V (which includes the three minor oxidation processes) show a GDE surface coverage by a seemingly amorphous layer (see Fig. 5.b). No toroidal particles are present at this state of charge. Nevertheless, crystalline Li_2O_2 is detected by XRD (see Fig. 2.a), which probably derives from the presence of large numbers of "donut"-shaped particles still visible inside the pores in Fig. 6.b). As the literature agrees on the fact that crystalline Li_2O_2 particles are electrochemically removed only at potentials higher than 3.5 V [26,63], their complete absence from the GDE surface is proposed to be due to an initial oxidation of Li_2O_2 to $Li_{2-x}O_2$. Therefore, the amorphous layer covering the GDE surface might be a product of the parasitic decomposition of DMSO by Li_2O_2 and/or $Li_{2-x}O_2$, such as LiOH [48,64,65]. The pores inside the electrode (although still largely blocked) seem less clogged than after discharge (see Fig. 6.b). As the product inside the pores is removed already at low potentials, it is likely the product of the surface growth pathway, i.e., amorphous Li_2O_2. This confirms the assumption that the surface growth pathway takes place predominantly in

the pores, whereas the solvated LiO_2 intermediates of the solution growth pathway move through the pores from the O_2 inlet to the GDE/separator side.

After the end of recharge at the cut-off potential of 4.15 V (now also including the three major high-potential oxidation reactions visible in Fig. 8.a) an apparently organic film covers the GDE surface (see Fig. 4.c) – an indication for the progressing DMSO decomposition at high potentials. The different morphology of the organic film compared to the surface layer observed in Fig. 4.b) points to a different reaction. This might be the DMSO decomposition by singlet O_2, which is formed by Li_2O_2 oxidation at potentials > 3.55 V. In the cross-section SEM images "donut"-shaped particles are still visible in the open pores, which indicates an incomplete (electro)chemical Li_2O_2 removal at the end of charge (see Fig. 6.c and the crystalline Li_2O_2 reflection after recharge in Fig. 2.b). In general the GDE seems less porous (i.e., the pores are smaller) in comparison to that at a potential of 3.6 V (see Fig. 6.c), which is most probably caused by deposition of solvent decomposition products inside the GDE pores. These observations are in good agreement with the incomplete recharge observed during the initial cycle. Because a large part of the crystalline Li_2O_2 is still present, the decomposition of DMSO at potentials > 3.6 V is likely related to the presence of singlet O_2, which was recently also suggested for ether-based electrolytes by Mahne *et al.* [37].

The differential capacity plots obtained from the first recharge with LiTFSI/TEGDME show one major and two minor oxidation processes below 3.6 V (see Fig. 8.b). These are observed at potentials of 3.1 V, 3.3 V and 3.5 V, which correspond to the minor processes taking place during charge with LiTFSI/DMSO. In good agreement with literature reports and previous observations in this work, oxidation reactions at potentials < 3.6 V are therefore assigned to the oxidation of amorphous Li_2O_2, as this compound is formed as major product in the TEGDME- and as minor product in the DMSO-based electrolyte. Similar to the case of

LiTFSI/DMSO, a major oxidation process takes place in a higher potential range from 3.7 V to 4.1 V during the initial recharge.

After recharge to 3.6 V with LiTFSI/TEGDME the GDE surface as well as pores look comparable to those after discharge: the surface layer is still present obscuring the view on the carbon particles of the GDE (see Fig. 5.b), and the porous structure of the GDE is still largely blocked (see Fig. 7.b). Therefore, the oxidation signals at potentials up to 3.6 V can be attributed to processes, which do not lead to an immediate product removal, e.g., the initial delithiation of amorphous Li_2O_2 to $Li_{2-x}O_2$ at the (not visible) Li_2O_2/electrode interface. This interpretation also supports reports by other groups that the electroactive interface changes from Li_2O_2/electrolyte (during discharge) to Li_2O_2/electrode (during charge) [66,67]. At this state of charge, the GDE surface also exhibits the presence of elongated particles with lengths of up to 1 µm (see Fig. 5.b), which are probably carbonate and/or carboxylate products from the chemical reactions of delithiated intermediates with the ether-based electrolyte and/or the carbon GDE [68–70].

Recharge to a potential of 4.15 V results in an active electrode surface recovery to an almost pristine state with products neither visible on the surface nor in the pores of the GDE (compare GDE surface and cross-section SEM images depicted in Figs. 5.c) and 7.c) to those of a pristine GDE in Fig. S2). The elongated particles, however, are still present on the GDE surface at the end of recharge. In a XRD and electron microscopical study with LiFSI/TEGDME Zhai *et al.* assigned recharge potentials > 3.5 V to the oxidation of Li_2O_2 [63]. This in combination with the observation of the start of CO_2 evolution during recharge with TEGDME-based electrolytes at potentials > 4.15 V by other groups [52,71] lead to two conclusions: (i) the elongated particles probably consist of Li_2CO_3, and (ii) the reactions taking place at potentials > 3.7 V in Fig. 8.b) can be assigned to Li_2O_2 oxidation.

In summary, the following processes take place during recharge: At low potentials (< 3.6 V) the (amorphous) products located in the GDE pores are partially removed when using LiTFSI/DMSO. Product removal is not observed with LiTFSI/TEGDME, so that an initial Li_2O_2 oxidation resulting in other solid products (e.g., $Li_{2-x}O_2$ and/or LiO_2) is most likely the prevailing process. The GDE surface products – most probably both Li_2O_2 as well as $Li_{2-x}O_2$ – lead to solvent decomposition already at low potentials, which in the case of DMSO result in an amorphous surface layer, with TEGDME in side product particles. At high potentials a clogging of the pores and an organic film on the GDE surface indicate progressing solvent decomposition with LiTFSI/DMSO, which is most likely due to the singlet O_2 evolving during Li_2O_2 oxidation at potentials > 3.55 V. In the case of LiTFSI/TEGDME an almost complete recovery of the active electrode surface by removal of the pore-clogging products and the residual surface film takes place by recharge to 4.15 V. However, also with TEGDME as solvent side product (particles) – attributed to Li_2CO_3 and/or carboxylates – are present on the GDE surface at the end of recharge.

In the second cycle, the considerably lower discharge capacity with LiTFSI/DMSO is provided by one high-potential reaction at ca. 2.77 V, which was also the case during the first discharge and attributed to O_2^-/solvated LiO_2 formation (see Fig. 8.a).

The GDE surface depicted in the SEM image in Fig. 4.d) is still covered by the organic DMSO decomposition product observed after first recharge. Although not clearly visible, the film apparently covers several "donut"-shaped particles of up to 350 nm. This observation and the presence of crystalline Li_2O_2 also after second discharge (see Fig. 2.a) are in good agreement with the similar discharge reaction potentials in the first and second discharge. However, the same reaction results in a significantly decreased second discharge capacity (see Fig. 1.b) as a

result of a blocked active electrode surface by DMSO decomposition products. Supporting this argumentation is the fact that the porous structure of the GDE is even more clogged after second discharge (see Fig. 6.d), which is the combined result of (i) incomplete discharge product removal as well as side product deposition during charge and (ii) renewed product formation at the remaining active electrode sites during second discharge. The SEM cross-sections depicted in Fig. 6 illustrate very well the reason for the capacity failure of LiTFSI/DMSO from the second discharge on.

During the subsequent recharge only one oxidation reaction is visible at a potential of 3.95 V followed by an intensity increase of the differential capacity from 4.05 V to 4.15 V (see Fig. 8.a). As discussed previously it is reasonable to believe that the increasing intensity at potentials ≥ 4.05 V is related to electrolyte decomposition.

The second discharge with the TEGDME-based electrolyte contains the high- and low-potential reactions at 2.70 V and 2.53 V already detected in the first discharge (see Fig. 8.b). Again, only small amounts of Li_2O_2 is present after full discharge (see Fig. 2.b).

Therefore, it is not surprising that the GDE surface after second discharge is completely covered by a film visually identical to that after first discharge – with the exception of elongated side product particles already observed during recharge at a potential of 3.6 V (see Fig. 5.d). These particles apparently accumulate during cycling, as they are present in larger numbers on the GDE surface after second discharge than during recharge. This can be attributed to the formation of carbonates and carboxylates during dis- and recharge as discussed above, and the fact that the cut-off potential of 4.15 V used in this work is below that needed for carbonate removal by oxidation [52,71]. The porous carbon network is again clogged after second discharge, this time, however, to a larger extent by bulk than by particle products (see Fig. 7.d).

The second recharge features oxidation reactions at potentials of 3.1 V as well as ca. 3.95 V and $\geq$ 4.05 V (see Fig. 8.b). The low-potential process has previously been assigned to the oxidation of the Li_2O_2 film in contact with the carbon electrode. The two latter oxidation reactions are attributed to the almost complete removal of the pore-clogging and residual surface film products thus leading to a recovery of the GDE pores and surface. Interestingly, the intensity decrease of the oxidation reaction at 3.1 V (assigned to initial Li_2O_2 oxidation) between first and second recharge is much smaller than that of the high-potential processes (assigned to active surface recovery). This implies that despite a continuously good initial Li_2O_2 oxidation step the electrochemical surface recovery is decreasing. Hence, the capacity fading during cycling can be attributed to two processes: (i) an accumulation of Li_2O_2 oxidation intermediates (e.g., $Li_{2-x}O_2$, LiO_2…) and (ii) chemical reactions of these compounds with the electrolyte or the GDE leading to an accumulation of side products, such as carbonate and carboxylates. As the latter is the more probable process due to the reactivity of the Li_2O_2 oxidation products, the better cycling stability with LiTFSI/TEGDME must be due to the higher reversibility of Li_2O_2 formation on the GDE surface and in the pores. The side reactions lead to different products, i.e., particle accumulation with LiTFSI/TEGDME and film formation with LiTFSI/DMSO. This results in a quicker electrode surface deactivation with the latter electrolyte due to a diffusion-limiting layer hindering the transport Li^+ ions and O_2 to active sites. This irreversible deactivation process already takes place during first recharge with LiTFSI/DMSO.

During the third and following discharge cycles the capacity decreases to negligible values with LiTFSI/DMSO (see Fig. 1.b). Two reduction processes are detected: one at a potential of 2.77 V, which is continuously decreasing in intensity, and one at a low potential of ca. 2.68 V (see Fig. 8.a). Hence, continued cycling results in an increasing contribution of the surface

growth pathway also when using the DMSO-based electrolyte, whereas the Li_2O_2 particle formation at high potentials *via* the solution growth pathway is decreasing. The observation of a low-potential process is attributed to the Li_2O_2 film formation, which was already taking place during the initial two cycles but is now also detected electrochemically due to the severely decreasing contribution of Li_2O_2 particle formation at high potentials. This assumption is supported by the CV measurements (see Fig. S1.a): during the cathodic sweep the high-potential peak current density decreases until a previously obscured low-potential process is visible from the second cycle on. This is probably the result of a shrinking active electrode surface due to the presence of the organic decomposition product film covering the GDE surface since first recharge.

During the third and following charge cycles no oxidation reactions except solvent decomposition processes at potentials > 4.05 V are detected, which indicates that battery cycling from the third cycle onward mainly results in DMSO oxidation.

The discharge/charge capacities decrease far less significantly following the second cycle when using TEGDME as a solvent (see Fig. 1.b). The reduction processes are observed at potentials comparable to those of the first two discharge cycles: one at high potentials of around 2.66 V, which is continuously decreasing in intensity, and one at 2.53 V (see Fig. 8.b). Hence, the discharge reactions do not change as much during the first five cycles with LiTFSI/TEGDME as with LiTFSI/DMSO.

The same is true for the low- and high-potential oxidation reactions during the third and following recharges, which are observed at potentials similar to those of the first two charge cycles with a comparably small decrease in intensity (see Fig. 8.b). This means that during recharge still the same processes are taking place: (i) an initial oxidation of the surface film and (ii) a complete film removal as well as pore recovery. Hence, the observed accumulation

of side product particles is proposed to be the main deactivation process during cycling with this electrolyte.

The continuity of discharge and charge processes over several cycles is probably also the main reason for the better cycling stability of the TEGDME- compared to the DMSO-based electrolyte. The predominant surface growth pathway in low-DN electrolytes results in a more reversible (amorphous) Li_2O_2 formation and is beneficial for recharge and cycling stability. This is also supported by the cycling experiments after LiTFSI replacement by $LiNO_3$ or $LiClO_4$ with TEGDME as solvent (see Fig. S6): The increased discharge capacities and potentials indicate at least partial changes in the reaction pathways from predominant surface film growth to solution particle growth. Additionally, the initially higher cycling stability obtained with LiTFSI/TEGDME decreases drastically as soon as the discharge pathway changes.

4. Conclusion

The investigations in this work give insight into the manifold reasons for the different electrochemical performances of LiTFSI/DMSO and LiTFSI/TEGDME, which are mainly attributed to the difference of (side) products formed during cycling. Whereas LiTFSI/DMSO exhibits significantly better initial electrochemical properties, the cycling stability is considerably better with LiTFSI/TEGDME.

Electron microscopic investigations in this work showed that the initial discharge capacity is largely influenced by the difference in Li_2O_2 growth pathways in both electrolytes. The predominating mechanisms with TEGDME and DMSO as solvents result in product films *via* adsorbed LiO_2 intermediates (surface growth pathway) and Li_2O_2 particles *via* solvated LiO_2

30

intermediates (solution growth pathway), respectively. At the beginning of discharge O_2 is reduced to O_2^- and forms LiO_2 close to the O_2 inlet. Whereas solvated LiO_2 can be transported away from the GDE's O_2 inlet side (with the LiO_2 concentration gradient as driving force), adsorbed LiO_2 is further reduced to Li_2O_2 at the initial adsorption site. These mechanisms lead to almost completely clogged pores close to the O_2 inlet, i.e., an earlier O_2 transport limitation, with the TEGDME-based electrolyte. Thus the active electrode sites of the porous GDE cannot be fully utilized, which leads to an earlier potential drop and a lower discharge capacity.

The higher cycling stability when using the LiTFSI/TEGDME electrolyte is proposed to have two reasons: First, the almost complete removal of the amorphous discharge product film during recharge. The toroidal and "donut"-shaped particles observed as major discharge product with the DMSO-based electrolyte, on the other hand, are still present in the pores after recharge. The second reason is the nature of the side products formed in the two electrolytes: SEM imaging showed that DMSO decomposition during the first recharge results in the formation of an organic film which covers the surface and clogs the pores of the GDE. With TEGDME as solvent, on the other hand, parasitic reactions result in the formation of side product particles. This particle formation and accumulation of side products around rather than film coverage of active sites is proposed to be a reason for the slower GDE surface deactivation with the TEGDME-based electrolyte. Furthermore, the unchanged number of electrochemical processes during continued cycling showed that the side product particles do not influence the nature of the occurring redox reactions. The organic layer present during initial recharge with DMSO as solvent, however, most likely prevents the quick O_2 reduction/LiO_2 solvation of the solution growth pathway in favor of continuous DMSO decomposition.

This work has provided insight into the effects of the location of discharge product formation in the GDE pores on the discharge capacity and the nature of side products on the cycling

stability. Further investigations are needed regarding both processes, especially on how to avoid side products as the main reason for early battery failure.

Associated content

The Supporting Information is available free of charge and contains a detailed discussion of LSV and CV measurements recorded with a scan rate of 0.1 mV s^{-1}, electron microscopic images depicting pristine GDEs as well as discharge product decomposition by the electron beam and cycling data of TEGDME-based electrolytes with different Li$^+$ conducting salts.

References

[1]   P.G. Bruce, S.A. Freunberger, L.J. Hardwick, J.-M. Tarascon, Li–O$_2$ and Li–S batteries with high energy storage, Nat. Mater. 11 (2012) 19–29. doi:10.1038/nmat3191.

[2]   X. Yao, Q. Dong, Q. Cheng, D. Wang, Why Do Lithium-Oxygen Batteries Fail: Parasitic Chemical Reactions and Their Synergistic Effect, Angew. Chemie Int. Ed. 55

(2016) 11344–11353. doi:10.1002/anie.201601783.

[3]   C.O. Laoire, S. Mukerjee, K.M. Abraham, E.J. Plichta, M.A. Hendrickson, Elucidating the mechanism of oxygen reduction for lithium-air battery applications, J. Phys. Chem. C. 113 (2009) 20127–20134. doi:10.1021/jp908090s.

[4]   C.O. Laoire, S. Mukerjee, K.M. Abraham, E.J. Plichta, M.A. Hendrickson, Influence of nonaqueous solvents on the electrochemistry of oxygen in the rechargeable lithium-air battery, J. Phys. Chem. C. 114 (2010) 9178–9186. doi:10.1021/jp102019y.

[5]   Y.-C. Lu, D.G. Kwabi, K.P.C. Yao, J.R. Harding, J. Zhou, L. Zuin, Y. Shao-Horn, The discharge rate capability of rechargeable Li– O_2 batteries, Energy Environ. Sci. 4 (2011) 2999. doi:10.1039/c1ee01500a.

[6]   B.D. McCloskey, D.S. Bethune, R.M. Shelby, T. Mori, R. Scheffler, A. Speidel, M. Sherwood, A.C. Luntz, Limitations in rechargeability of Li-O_2 batteries and possible origins, J. Phys. Chem. Lett. 3 (2012) 3043–3047. doi:10.1021/jz301359t.

[7]   C.O. Laoire, S. Mukerjee, E.J. Plichta, M.A. Hendrickson, K.M. Abraham, Rechargeable Lithium/TEGDME-LiPF$_6$/O_2 Battery, J. Electrochem. Soc. 158 (2011) A302. doi:10.1149/1.3531981.

[8]   Z. Peng, S.A. Freunberger, L.J. Hardwick, Y. Chen, V. Giordani, F. Bardé, P. Novák, D. Graham, J.M. Tarascon, P.G. Bruce, Oxygen reactions in a non-aqueous Li$^+$ electrolyte, Angew. Chemie - Int. Ed. 50 (2011) 6351–6355. doi:10.1002/anie.201100879.

[9]   W. Xu, K. Xu, V. V. Viswanathan, S.A. Towne, J.S. Hardy, J. Xiao, Z. Nie, D. Hu, D. Wang, J.G. Zhang, Reaction mechanisms for the limited reversibility of Li-O_2 chemistry in organic carbonate electrolytes, J. Power Sources. 196 (2011) 9631–9639.

doi:10.1016/j.jpowsour.2011.06.099.

[10] L.J. Hardwick, P.G. Bruce, The pursuit of rechargeable non-aqueous lithium-oxygen battery cathodes, Curr. Opin. Solid State Mater. Sci. 16 (2012) 178–185. doi:10.1016/j.cossms.2012.04.001.

[11] J. Wang, Y. Li, X. Sun, Challenges and opportunities of nanostructured materials for aprotic rechargeable lithium-air batteries, Nano Energy. 2 (2013) 443–467. doi:10.1016/j.nanoen.2012.11.014.

[12] S. Meini, N. Tsiouvaras, K.U. Schwenke, M. Piana, H. Beyer, L. Lange, H.A. Gasteiger, Rechargeability of Li-air cathodes pre-filled with discharge products using an ether-based electrolyte solution: Implications for cycle-life of Li-air cells, Phys. Chem. Chem. Phys. 15 (2013) 11478–11493. doi:10.1039/c3cp51112j.

[13] T. Ogasawara, A. Débart, M. Holzapfel, P. Novák, P.G. Bruce, Rechargeable Li_2O_2 Electrode for Lithium Batteries, J. Am. Chem. Soc. 128 (2006) 1390–1393. doi:10.1021/ja056811q.

[14] D. Sharon, D. Hirshberg, M. Afri, A. Garsuch, A.A. Frimer, D. Aurbach, Lithium–Oxygen Electrochemistry in Non-Aqueous Solutions, Isr. J. Chem. 55 (2015) 508–520. doi:10.1002/ijch.201400135.

[15] D. Xu, Z. Wang, J. Xu, L. Zhang, X. Zhang, Novel DMSO-based electrolyte for high performance rechargeable Li–O_2 batteries, Chem. Commun. 48 (2012) 6948. doi:10.1039/c2cc32844e.

[16] X. Lin, X. Lu, T. Huang, Z. Liu, A. Yu, Binder-free nitrogen-doped carbon nanotubes electrodes for lithium-oxygen batteries, J. Power Sources. 242 (2013) 855–859. doi:10.1016/j.jpowsour.2013.05.100 Short communication.

[17] M.J. Trahan, S. Mukerjee, E.J. Plichta, M.A. Hendrickson, K.M. Abraham, Studies of Li-Air Cells Utilizing Dimethyl Sulfoxide-Based Electrolyte, J. Electrochem. Soc. 160 (2012) A259–A267. doi:10.1149/2.048302jes.

[18] F. Bardé, Y. Chen, L. Johnson, S. Schaltin, J. Fransaer, P.G. Bruce, Sulfone-based electrolytes for nonaqueous Li-O_2 batteries, J. Phys. Chem. C. 118 (2014) 18892–18898. doi:10.1021/jp5048198.

[19] S.E. Herrera, A.Y. Tesio, R. Clarenc, E.J. Calvo, AFM study of oxygen reduction products on HOPG in the $LiPF_6$-DMSO electrolyte, Phys. Chem. Chem. Phys. 16 (2014) 9925–9929. doi:10.1039/c3cp54621g.

[20] L. Johnson, C. Li, Z. Liu, Y. Chen, S.A. Freunberger, P.C. Ashok, B.B. Praveen, K. Dholakia, J.-M. Tarascon, P.G. Bruce, The role of LiO_2 solubility in O_2 reduction in aprotic solvents and its consequences for Li–O_2 batteries, Nat. Chem. 6 (2014) 1091–1099. doi:10.1038/nchem.2101.

[21] W. Fan, Z. Cui, X. Guo, Tracking formation and decomposition of abacus-ball-shaped lithium peroxides in Li-O_2 cells, J. Phys. Chem. C. 117 (2013) 2623–2627. doi:10.1021/jp310765s.

[22] R.R. Mitchell, B.M. Gallant, Y. Shao-Horn, C. V. Thompson, Mechanisms of Morphological Evolution of Li_2O_2 Particles during Electrochemical Growth, J. Phys. Chem. Lett. 4 (2013) 1060–1064. doi:10.1021/jz4003586.

[23] C. Xia, M. Waletzko, L. Chen, K. Peppler, P.J. Klar, J. Janek, Evolution of Li_2O_2 Growth and Its Effect on Kinetics of Li–O_2 Batteries, ACS Appl. Mater. Interfaces. 6 (2014) 12083–12092. doi:10.1021/am5010943.

[24] D. Aurbach, B.D. McCloskey, L.F. Nazar, P.G. Bruce, Advances in understanding

mechanisms underpinning lithium–air batteries, Nat. Energy. 1 (2016) 16128. doi:10.1038/nenergy.2016.128.

[25] D.G. Kwabi, M. Tułodziecki, N. Pour, D.M. Itkis, C. V. Thompson, Y. Shao-Horn, Controlling Solution-Mediated Reaction Mechanisms of Oxygen Reduction Using Potential and Solvent for Aprotic Lithium–Oxygen Batteries, J. Phys. Chem. Lett. 7 (2016) 1204–1212. doi:10.1021/acs.jpclett.6b00323.

[26] B.D. Adams, C. Radtke, R. Black, M.L. Trudeau, K. Zaghib, L.F. Nazar, Current density dependence of peroxide formation in the Li–O_2 battery and its effect on charge, Energy Environ. Sci. 6 (2013) 1772. doi:10.1039/c3ee40697k.

[27] Y. Zhang, X. Zhang, J. Wang, W.C. McKee, Y. Xu, Z. Peng, Potential-Dependent Generation of O_2^- and LiO_2 and Their Critical Roles in O_2 Reduction to Li_2O_2 in Aprotic Li–O_2 Batteries, J. Phys. Chem. C. 120 (2016) 3690–3698. doi:10.1021/acs.jpcc.5b12338.

[28] D. Sharon, V. Etacheri, A. Garsuch, M. Afri, A.A. Frimer, D. Aurbach, On the challenge of electrolyte solutions for Li-air batteries: Monitoring oxygen reduction and related reactions in polyether solutions by spectroscopy and EQCM, J. Phys. Chem. Lett. 4 (2013) 127–131. doi:10.1021/jz3017842.

[29] H.-K. Lim, H.-D. Lim, K.-Y. Park, D.-H. Seo, H. Gwon, J. Hong, W.A. Goddard, H. Kim, K. Kang, Toward a Lithium–"Air" Battery: The Effect of CO_2 on the Chemistry of a Lithium–Oxygen Cell, J. Am. Chem. Soc. 135 (2013) 9733–9742. doi:10.1021/ja4016765.

[30] N.B. Aetukuri, B.D. McCloskey, J.M. Garciá, L.E. Krupp, V. Viswanathan, A.C. Luntz, Solvating additives drive solution-mediated electrochemistry and enhance toroid growth in non-aqueous Li-O_2 batteries, Nat. Chem. 7 (2015) 50–56.

doi:10.1038/nchem.2132.

[31]   M. Augustin, D. Fenske, J. Parisi, Study on Electrolyte Stability and Oxygen

        Reduction Reaction Mechanisms in the Presence of Manganese Oxide Catalysts for

        Aprotic Lithium–Oxygen Batteries, Energy Technol. 4 (2016) 1531–1542.

        doi:10.1002/ente.201600115.

[32]   Y. Zhang, Q. Cui, X. Zhang, W.C. McKee, Y. Xu, S. Ling, H. Li, G. Zhong, Y. Yang,

        Z. Peng, Amorphous Li_2O_2 : Chemical Synthesis and Electrochemical Properties,

        Angew. Chemie Int. Ed. 55 (2016) 10717–10721. doi:10.1002/anie.201605228.

[33]   B.M. Gallant, D.G. Kwabi, R.R. Mitchell, J. Zhou, C. V. Thompson, Y. Shao-Horn,

        Influence of Li_2O_2 morphology on oxygen reduction and evolution kinetics in $Li–O_2$

        batteries, Energy Environ. Sci. 6 (2013) 2518. doi:10.1039/c3ee40998h.

[34]   S. Ganapathy, B.D. Adams, G. Stenou, M.S. Anastasaki, K. Goubitz, X.-F. Miao, L.F.

        Nazar, M. Wagemaker, Nature of Li_2O_2 Oxidation in a $Li–O_2$ Battery Revealed by

        Operando X-ray Diffraction, J. Am. Chem. Soc. 136 (2014) 16335–16344.

        doi:10.1021/ja508794r.

[35]   L. Luo, B. Liu, S. Song, W. Xu, J.-G. Zhang, C. Wang, Revealing the reaction

        mechanisms of $Li–O_2$ batteries using environmental transmission electron microscopy,

        Nat. Nanotechnol. 12 (2017) 535–539. doi:10.1038/nnano.2017.27.

[36]   J. Wandt, P. Jakes, J. Granwehr, H.A. Gasteiger, R.A. Eichel, Singlet Oxygen

        Formation during the Charging Process of an Aprotic Lithium-Oxygen Battery,

        Angew. Chemie - Int. Ed. 55 (2016) 6892–6895. doi:10.1002/anie.201602142.

[37]   N. Mahne, B. Schafzahl, C. Leypold, M. Leypold, S. Grumm, A. Leitgeb, G.A.

        Strohmeier, M. Wilkening, O. Fontaine, D. Kramer, C. Slugovc, S.M. Borisov, S.A.

Freunberger, Singlet oxygen generation as a major cause for parasitic reactions during cycling of aprotic lithium–oxygen batteries, Nat. Energy. 2 (2017) 17036. doi:10.1038/nenergy.2017.36.

[38]   H. Geaney, C. O'Dwyer, Tailoring Asymmetric Discharge-Charge Rates and Capacity Limits to Extend Li-O$_2$ Battery Cycle Life, ChemElectroChem. 4 (2017) 628–635. doi:10.1002/celc.201600662.

[39]   R.W.G. Wyckoff, Crystal Structures, Vol. 1, 2nd ed., Interscience Publishers, New York, London, Sydney, 1963.

[40]   S.L. Mair, The electron distribution of the hydroxide ion in lithium hydroxide, Acta Crystallogr. Sect. A. 34 (1978) 542–547. doi:10.1107/S0567739478001151.

[41]   L. Xue, C.W. Padgett, D.D. DesMarteau, W.T. Pennington, Synthesis and structures of alkali metal salts of bis[(trifluoromethyl)sulfonyl]imide, Solid State Sci. 4 (2002) 1535–1545. doi:10.1016/S1293-2558(02)00050-X.

[42]   C. Ling, R. Zhang, K. Takechi, F. Mizuno, Intrinsic Barrier to Electrochemically Decompose Li$_2$CO$_3$ and LiOH, J. Phys. Chem. C. 118 (2014) 26591–26598. doi:10.1021/jp5093306.

[43]   Z. Li, S. Ganapathy, Y. Xu, J.R. Heringa, Q. Zhu, W. Chen, M. Wagemaker, Understanding the Electrochemical Formation and Decomposition of Li$_2$O$_2$ and LiOH with Operando X-ray Diffraction, Chem. Mater. 29 (2017) 1577–1586. doi:10.1021/acs.chemmater.6b04370.

[44]   R.A. Wong, C. Yang, A. Dutta, M. O, M. Hong, M.L. Thomas, K. Yamanaka, T. Ohta, K. Waki, H.R. Byon, Critically Examining the Role of Nanocatalysts in Li–O$_2$ Batteries: Viability toward Suppression of Recharge Overpotential, Rechargeability,

and Cyclability, ACS Energy Lett. 3 (2018) 592–597. doi:10.1021/acsenergylett.8b00054.

[45] B.D. McCloskey, A. Speidel, R. Scheffler, D.C. Miller, V. Viswanathan, J.S. Hummelshøj, J.K. Nørskov, A.C. Luntz, Twin problems of interfacial carbonate formation in nonaqueous Li-O$_2$ batteries, J. Phys. Chem. Lett. 3 (2012) 997–1001. doi:10.1021/jz300243r.

[46] M.M. Ottakam Thotiyl, S.A. Freunberger, Z. Peng, P.G. Bruce, The Carbon Electrode in Nonaqueous Li–O$_2$ Cells, J. Am. Chem. Soc. 135 (2013) 494–500. doi:10.1021/ja310258x.

[47] A.I. Belova, D.G. Kwabi, L.V. Yashina, Y. Shao-Horn, D.M. Itkis, Mechanism of Oxygen Reduction in Aprotic Li-Air Batteries: The Role of Carbon Electrode Surface Structure, J. Phys. Chem. C 121 (2017) 1569−1577. doi:10.1021/acs.jpcc.6b12221.

[48] F. Marchini, S. Herrera, W. Torres, A.Y. Tesio, F.J. Williams, E.J. Calvo, Surface Study of Lithium-Air Battery Oxygen Cathodes in Different Solvent-Electrolyte pairs, Langmuir. 31 (2015) 9236–9245. doi:10.1021/acs.langmuir.5b02130.

[49] D.G. Kwabi, T.P. Batcho, C. V. Amanchukwu, N. Ortiz-Vitoriano, P. Hammond, C. V Thompson, Y. Shao-Horn, Chemical Instability of Dimethyl Sulfoxide in Lithium–Air Batteries, J. Phys. Chem. Lett. 5 (2014) 2850–2856. doi:10.1021/jz5013824.

[50] S.A. Freunberger, Y. Chen, N.E. Drewett, L.J. Hardwick, F. Bardé, P.G. Bruce, The lithium-oxygen battery with ether-based electrolytes, Angew. Chemie Int. Ed. 50 (2011) 8609–8613. doi:10.1002/anie.201102357.

[51] C.C. Li, W. Zhang, H. Ang, H. Yu, B.Y. Xia, X. Wang, Y.H. Yang, Y. Zhao, H.H. Hng, Q. Yan, Compressed hydrogen gas-induced synthesis of Au-Pt core-shell

nanoparticle chains towards high-performance catalysts for Li-O$_2$ batteries, J. Mater. Chem. A. 2 (2014) 10676–10681. doi:10.1039/c4ta01475h.

[52] R.A. Wong, A. Dutta, C. Yang, K. Yamanaka, T. Ohta, A. Nakao, K. Waki, H.R. Byon, Structurally Tuning Li$_2$O$_2$ by Controlling the Surface Properties of Carbon Electrodes: Implications for Li–O$_2$ Batteries, Chem. Mater. 28 (2016) 8006–8015. doi:10.1021/acs.chemmater.6b03751.

[53] B.D. McCloskey, R. Scheffler, A. Speidel, G. Girishkumar, A.C. Luntz, On the mechanism of nonaqueous Li-O$_2$ electrochemistry on C and its kinetic overpotentials: Some implications for Li-air batteries, J. Phys. Chem. C. 116 (2012) 23897–23905. doi:10.1021/jp306680f.

[54] N.B. Aetukuri, G.O. Jones, L.E. Thompson, C. Ozgit-Akgun, E. Akca, G. Demirci, H.-C. Kim, D.S. Bethune, K. Virwani, G.M. Wallraff, Ion-Pairing Limits Crystal Growth in Metal-Oxygen Batteries, (2018). http://arxiv.org/abs/1807.03840 (accessed September 13, 2018).

[55] W.H. Ryu, F.S. Gittleson, M. Schwab, T. Goh, A.D. Taylor, A mesoporous catalytic membrane architecture for lithium-oxygen battery systems, Nano Lett. 15 (2015) 434–441. doi:10.1021/nl503760n.

[56] K.-H. Xue, T.-K. Nguyen, A.A. Franco, Impact of the Cathode Microstructure on the Discharge Performance of Lithium Air Batteries: A Multiscale Model, J. Electrochem. Soc. 161 (2014) E3028–E3035. doi:10.1149/2.002408jes.

[57] K.-H. Xue, E. McTurk, L. Johnson, P.G. Bruce, A.A. Franco, A Comprehensive Model for Non-Aqueous Lithium Air Batteries Involving Different Reaction Mechanisms, J. Electrochem. Soc. 162 (2015) A614–A621. doi:10.1149/2.0121504jes.

[58] D.G. Kwabi, V.S. Bryantsev, T.P. Batcho, D.M. Itkis, C. V. Thompson, Y. Shao-Horn, Experimental and Computational Analysis of the Solvent-Dependent O_2/Li^+-O_2^- Redox Couple: Standard Potentials, Coupling Strength, and Implications for Lithium-Oxygen Batteries, Angew. Chemie Int. Ed. 55 (2016) 3129–3134. doi:10.1002/anie.201509143.

[59] C.M. Burke, V. Pande, A. Khetan, V. Viswanathan, B.D. McCloskey, Enhancing electrochemical intermediate solvation through electrolyte anion selection to increase nonaqueous $Li–O_2$ battery capacity, Proc. Natl. Acad. Sci. 112 (2015) 9293–9298. doi:10.1073/pnas.1505728112.

[60] D. Sharon, D. Hirsberg, M. Salama, M. Afri, A.A. Frimer, M. Noked, W. Kwak, Y.-K. Sun, D. Aurbach, Mechanistic Role of Li^+ Dissociation Level in Aprotic $Li–O_2$ Battery, ACS Appl. Mater. Interfaces. 8 (2016) 5300–5307. doi:10.1021/acsami.5b11483.

[61] M. Iliksu, A. Khetan, S. Yang, U. Simon, H. Pitsch, D.U. Sauer, Elucidation and Comparison of the Effect of LiTFSI and $LiNO_3$ Salts on Discharge Chemistry in Nonaqueous $Li–O_2$ Batteries, ACS Appl. Mater. Interfaces. 9 (2017) 19319–19325. doi:10.1021/acsami.7b03592.

[62] W. Linert, A. Camard, M. Armand, C. Michot, Anions of low Lewis basicity for ionic solid state electrolytes, Coord. Chem. Rev. 226 (2002) 137–141. doi:10.1016/S0010-8545(01)00416-7.

[63] D. Zhai, K.C. Lau, H.-H. Wang, J. Wen, D.J. Miller, J. Lu, F. Kang, B. Li, W. Yang, J. Gao, E. Indacochea, L.A. Curtiss, K. Amine, Interfacial Effects on Lithium Superoxide Disproportionation in $Li-O_2$ Batteries, Nano Lett. 15 (2015) 1041–1046. doi:10.1021/nl503943z.

[64]   D. Sharon, M. Afri, M. Noked, A. Garsuch, A.A. Frimer, D. Aurbach, Oxidation of Dimethyl Sulfoxide Solutions by Electrochemical Reduction of Oxygen, J. Phys. Chem. Lett. 4 (2013) 3115–3119. doi:10.1021/jz4017188.

[65]   T. Laino, A. Curioni, Chemical reactivity of aprotic electrolytes on a solid Li_2O_2 surface: screening solvents for Li–air batteries, New J. Phys. 15 (2013) 095009. doi:10.1088/1367-2630/15/9/095009.

[66]   J. Wang, Y. Zhang, L. Guo, E. Wang, Z. Peng, Identifying Reactive Sites and Transport Limitations of Oxygen Reactions in Aprotic Lithium-O_2 Batteries at the Stage of Sudden Death, Angew. Chemie - Int. Ed. 55 (2016) 5201–5205. doi:10.1002/anie.201600793.

[67]   J. Huang, B. Tong, Z. Li, T. Zhou, J. Zhang, Z. Peng, Probing the Reaction Interface in Li–Oxygen Batteries Using Dynamic Electrochemical Impedance Spectroscopy: Discharge–Charge Asymmetry in Reaction Sites and Electronic Conductivity, J. Phys. Chem. Lett. 9 (2018) 3403–3408. doi:10.1021/acs.jpclett.8b01351.

[68]   M. Carboni, S. Brutti, A.G. Marrani, Surface Reactivity of a Carbonaceous Cathode in a Lithium Triflate/Ether Electrolyte-Based Li–O_2 Cell, ACS Appl. Mater. Interfaces. 7 (2015) 21751–21762. doi:10.1021/acsami.5b05202.

[69]   A. Guéguen, P. Novák, E.J. Berg, XPS Study of the Interface Evolution of Carbonaceous Electrodes for Li-O_2 Batteries during the 1st Cycle, J. Electrochem. Soc. 163 (2016) A2545–A2550. doi:10.1149/2.0351613jes.

[70]   D. Giacco, M. Carboni, S. Brutti, A.G. Marrani, Noticeable Role of TFSI− Anion in the Carbon Cathode Degradation of Li–O_2 Cells, ACS Appl. Mater. Interfaces. 9 (2017) 31710–31720. doi:10.1021/acsami.7b05153.

[71] D.W. Kim, S.M. Ahn, J. Kang, J. Suk, H.K. Kim, Y. Kang, In situ real-time and quantitative investigation on the stability of non-aqueous lithium oxygen battery electrolytes, J. Mater. Chem. A. 4 (2016) 6332–6341. doi:10.1039/C6TA00371K.